AGU PUBLICATIONS

JGR

Journal of Geophysical Research: Earth Surface

RESEARCH ARTICLE
10.1002/2015JF003759

Key Points:
- High-resolution topographic data permit better glacier ice aerodynamic roughness (z_0) estimates
- Spatial z_0 variability over 3 orders of magnitude with different temporal trajectories
- Glacier topographic roughness used to upscale z_0 measurements for distributed ablation modeling

Supporting Information:
- Supporting Information S1

Correspondence to:
M. W. Smith,
m.w.smith@leeds.ac.uk

Citation:
Smith, M. W., D. J. Quincey, T. Dixon, R. G. Bingham, J. L. Carrivick, T. D. L. Irvine-Fynn, and D. M. Rippin (2016), Aerodynamic roughness of glacial ice surfaces derived from high-resolution topographic data, *J. Geophys. Res. Earth Surf.*, *121*, 748–766, doi:10.1002/2015JF003759.

Received 12 OCT 2015
Accepted 25 MAR 2016
Accepted article online 1 APR 2016
Published online 28 APR 2016

Aerodynamic roughness of glacial ice surfaces derived from high-resolution topographic data

Mark W. Smith[1], Duncan J. Quincey[1], Timothy Dixon[2], Robert G. Bingham[3], Jonathan L. Carrivick[1], Tristram D. L. Irvine-Fynn[4], and David M. Rippin[5]

[1]School of Geography and water@leeds, University of Leeds, Leeds, UK, [2]School of Earth and Environment, University of Leeds, Leeds, UK, [3]School of GeoSciences, University of Edinburgh, Edinburgh, UK, [4]Centre for Glaciology, Department for Geography and Earth Sciences, Aberystwyth University, Aberystwyth, UK, [5]Environment Department, University of York, York, UK

Abstract This paper presents new methods of estimating the aerodynamic roughness (z_0) of glacier ice directly from three-dimensional point clouds and digital elevation models (DEMs), examines temporal variability of z_0, and presents the first fully distributed map of z_0 estimates across the ablation zone of an Arctic glacier. The aerodynamic roughness of glacier ice surfaces is an important component of energy balance models and meltwater runoff estimates through its influence on turbulent fluxes of latent and sensible heat. In a warming climate these fluxes are predicted to become more significant in contributing to overall melt volumes. Ice z_0 is commonly estimated from measurements of ice surface microtopography, typically from topographic profiles taken perpendicular to the prevailing wind direction. Recent advances in surveying permit rapid acquisition of high-resolution topographic data allowing revision of assumptions underlying conventional z_0 measurement. Using Structure from Motion (SfM) photogrammetry with Multi-View Stereo (MVS) to survey ice surfaces with millimeter-scale accuracy, z_0 variation over 3 orders of magnitude was observed. Different surface types demonstrated different temporal trajectories in z_0 through 3 days of intense melt. A glacier-scale 2 m resolution DEM was obtained through terrestrial laser scanning (TLS), and subgrid roughness was significantly related to plot-scale z_0. Thus, we show for the first time that glacier-scale TLS or SfM-MVS surveys can characterize z_0 variability over a glacier surface potentially leading to distributed representations of z_0 in surface energy balance models.

1. Introduction

In glacier surface energy balance models, turbulent fluxes of sensible and latent heat are generally considered to be secondary to radiative heat fluxes [*Hock*, 2005]. However, they become increasingly influential (up to 80%) in overcast and windy conditions [*Holmgren*, 1971; *Marcus et al*., 1984; *Giesen et al*., 2014] and for glacierized regions characterized by maritime climates [*Hay and Fitzharris*, 1988; *Ishikawa et al*., 1992]. Critically, their relative contribution to overall ice surface mass loss is predicted to become more significant in a warming climate [*Braithwaite and Olesen*, 1990], making it imperative that the key influences on turbulent fluxes are better understood. One of the most important of these influences is the aerodynamic roughness height z_0, which is related to ice surface topographic roughness, in a complex way. Improved characterization of z_0 on glacier ice surfaces forms the focus of this paper.

All ice melt models which aim explicitly to incorporate turbulent fluxes, in some way incorporate a value, or range of values, for aerodynamic roughness height, z_0. This is because, in the absence of direct eddy correlation measurements (which are difficult to obtain in the field [*Greuell and Genthon*, 2004]), aerodynamic roughness height underpins the derivation of exchange coefficients for potential temperature and specific humidity in the surface boundary layer. These coefficients are often used to approximate turbulent fluxes using the bulk aerodynamic method [*Hock*, 2005; *Brock et al*., 2010]. However, z_0 is difficult to measure directly, and a range of different approximations are used. For example, spatially distributed surface energy balance models assume a uniform and constant value of z_0 [*Arnold et al*., 2006] and z_0 is also used as an optimized parameter in the fitting of model output to observations of glacier melt [*Hock and Holmgren*, 2005].

Uncertainty in z_0 values presents a serious challenge in the calculation of ice ablation with an order of magnitude change in z_0 leading to a factor of 2 change in estimated turbulent fluxes [*Munro*, 1989;

Hock and Holmgren, 1996; *Brock et al*., 2010]. Yet field studies have highlighted the variability of z_0 over ice surfaces in both space and time. *Brock et al*. [2006] summarize z_0 values for ice in the published literature, from 0.007 mm for Antarctic blue ice [*Bintanja and van den Broeke*, 1994, 1995] to 80 mm for very rough glacier ice [*Smeets et al*., 1999]. While values over smooth ice are ~0.1 mm, the majority of glacier ice z_0 values are in the range of 1–5 mm [*Brock et al*., 2006]. Ablation zones of glaciers can exhibit a large range of ice surface roughness features; however, attempts to model variations in z_0 over single valley glaciers to inform upscaling have proven unsuccessful [*Brock et al*., 2006]. Considering temporal variability of z_0, systematic increases in z_0 through the ablation season are observed on snow surfaces [*Arnold and Rees*, 2003; *Brock et al*., 2006; *Fassnacht et al*., 2009b]. However, such systematic increase is less pronounced on glacier ice which exhibits greater temporal variability in z_0 [*Müller and Keeler*, 1969; *Smeets et al*., 1999; *Denby and Smeets*, 2000; *Greuell and Smeets*, 2001; *Brock et al*., 2006; *Smeets and van den Broeke*, 2008]. Such temporal variability remains poorly quantified or constrained.

The calculation of z_0 from ice surface topography has retained assumptions put in place under conditions of limited topographic data and computational power. The aim of this paper is to address this shortcoming through application of recent advances in high-resolution surveying to estimate z_0 from ice surface topography. Specifically, we aim to (1) describe novel parameterizations of surface roughness to represent z_0 that utilize greater availability of high-resolution survey data; (2) examine the spatial variability of ice z_0 over the ablation zone of a small Arctic glacier using Structure from Motion; (3) investigate the possibility of upscaling microtopographic z_0 measurements to the glacier scale using Terrestrial Laser Scanning; and (4) characterize the temporal variability of z_0 as ice melt takes place over several days.

2. Meaning and Measurement of z_0

Aerodynamic roughness height, z_0, is defined herein as a length scale that characterizes the loss of wind momentum attributable to surface roughness [*Chappell and Heritage*, 2007], i.e., the height above the ground surface at which the extrapolated horizontal wind velocity drops to 0. The term arises as a constant of integration from the fitting of logarithmic profiles to velocity data as specified by boundary layer theory [*Prandtl*, 1926; *Millikan*, 1938] and is estimated for both water and air flows over a wide range of surface types [*Smith*, 2014]. Thus, under some (rough) flow conditions z_0 is a function of both surface and flow properties as indicated by wind tunnel experiments observing an increase of z_0 with free-stream velocity (or shear velocity) over the same gravel surface where faster aerodynamically rough flows transfer more momentum to the near surface [*Dong et al*., 2002]. In practice, z_0 is at least weakly related to surface properties, and relationships between z_0 and microtopography are exploited frequently to obtain z_0 values.

With z_0 defined as a property of the air flow, velocity-profile-based measurement would seem preferable; however, there are a number of inherent difficulties in adopting this approach. Detailed wind velocity profile measurements over sufficient durations are not always available [e.g., *Brock et al*., 2006; *Rees and Arnold*, 2006]. Data requirements are certainly too onerous for distributed measurement of z_0 in this way. Moreover, z_0 values derived from least squares model fit to velocity measurements are sensitive to instrumental errors [*Sicart et al*., 2014]. On glaciers, temperature inversions and katabatic winds often result in a wind speed maximum several meters above the surface [e.g., *Wallén*, 1948; *Denby and Greuell*, 2000; *Giesen et al*., 2014; *Sicart et al*., 2014] and thus deviate from the theoretical profile. Wind velocity profiles need to be adjusted for surface layer stability, and definition of the surface height above which velocity profiles are measured is not straightforward, particularly over rough surfaces [*Sullivan and Greeley*, 1993; *Smeets et al*., 1999; *Sicart et al*., 2014]. Displacement heights are often defined to account for mutual sheltering through addition of a height adjustment to velocity profiles that represents a uniform distribution of the aggregate volume of roughness elements and their wakes [*Smith*, 2014]. However, there is some uncertainty as to the appropriate level of the zero-reference plane [*Munro*, 1989; *Andreas*, 2002].

Estimations of z_0 from surface microtopography show good agreement with velocity-profile-derived z_0 values [*MacKinnon et al*., 2004]. From wind tunnel experiments on sand surfaces, grain size approaches have been developed [*Bagnold*, 1941] where z_0 is quantified as 1/30 of a grain diameter. This classic approach is inappropriate for complex ice and snow surfaces that are not composed of individual grains and exhibit

multiple scales of topographic variability. An equation developed by *Lettau* [1969] is used more frequently in studies on ice surfaces, where z_0 is quantified as

$$z_0 = 0.5h^*\left(\frac{s}{S}\right), \quad (1)$$

where h^* represents the average vertical extent of microtopographic variations (i.e., effective obstacle height, m), s is the silhouette area facing upwind (i.e., the roughness frontal area, m^2), and S is the unit ground area occupied by each element (i.e., the "lot" area, m^2). The drag coefficient is represented by an "average" drag coefficient of 0.5. The Lettau equation was developed from experiments placing several hundred bushel baskets in a field upwind of an anemometer mast. With such isolated and well-defined roughness elements, specification of each term in (1) is relatively straightforward and results agreed with velocity-profile-based z_0 values to ± 25%. However, on ice surfaces, both velocity profiles and surface roughness are more difficult to measure. Good agreement among eddy covariance, wind velocity profile, and microtopographic measurement techniques over ice is often reported [e.g., *Brock et al*., 2006], though differences are also apparent. For example, *van den Broeke* [1996] observed little agreement between the velocity profile and microtopographic methods, calculating a z_0 of 0.8 mm from wind velocity profiles and 120 mm using the Lettau equation (the latter of which was more realistic for the energy balance [*Hock*, 2005]).

Alternatives to (1) do exist; for example, *Sellers* [1965] estimates z_0 from h^* alone, calibrating a power-law relationship empirically. Meanwhile, *Counihan* [1971] and *Fryrear* [1985] use the plan area of roughness elements in place of the frontal area, and *Theurer* [1973] developed an equation that uses both metrics. *Banke and Smith* [1973] and *Andreas* [2011] integrate the Fourier transform of elevations for wavelengths $<$13 m to relate ice roughness to z_0. A common simplification of the Lettau equation for complex roughness fields encountered on ice was developed by *Munro* [1989] (section 3.4) and applied to topographic profiles perpendicular to the wind direction. However, sheltering effects from upwind are not taken into account and the ability of single profiles to represent roughness accurately is questionable.

High-resolution topographic data of glacier surfaces are increasingly available [e.g., *Nield et al*., 2012]. From a digital elevation model (DEM) the variability of z_0 for different profiles within the DEM can be reported [*Irvine-Fynn et al*., 2014]. Yet with advances in surveying techniques and computational power, the advantages of the *Munro* [1989] method in terms of minimal data requirements and computational efficiency have become less relevant. Indeed, estimation of z_0 using profile-based methods results in much of the potentially useful topographic data in three-dimensional point clouds of ice surfaces being discarded and does not make full use of this rich topographic data source [*Passalacqua et al*., 2015]. It is this shortcoming that we seek to address, through the analysis of multiple point clouds derived from Kårsaglaciären, a small glacier in northern Sweden.

3. Methods and Field Site

3.1. Field Site

Kårsaglaciären (68.358739°N, 18.323593°E) is a small (~1 km^2) mountain glacier located in the Vuoittasrita massif, part of the Abisko mountains, on the border between arctic Sweden and Norway. It presently terminates at ~ 900 m above sea level into a small ice-marginal lake that is developing as the ice margin retreats from a bedrock ridge. Since around 1912 the glacier has been in a state of near-constant retreat but with some isolated areas of minor advance noted [*Karlén*, 1973; *Bodin*, 1993]. Since the early 1940s the glacier has been included in the Swedish national mass balance program [*Ahlmann and Tryselius*, 1929; *Wallén*, 1948, 1949, 1959; *Karlén*, 1973; *Bodin*, 1993]. Climatic conditions at Kårsa are split between maritime (winter) and continental (summer), and dominant winds are katabatic (ice flow parallel). *Wallén* [1948, 1949] estimated that turbulent fluxes were responsible for ~40% of ablation at Kårsa.

3.2. Field Data Collection

3.2.1. Large-Scale DEMs From Terrestrial Laser Scanning

The ablation zone of Kårsaglaciären was surveyed in July 2013 using a RIEGL VZ-1000 terrestrial laser scanner (TLS). While the maximum range of the instrument is stated to be 1400 m [*RIEGL*, 2012], absorbance of the narrow class 1 infrared laser beam over the wet ice surface reduced the observed maximum range here to ~ 400 m on wet ice surfaces. The theoretical data acquisition rate was 100,000 points per second, but again

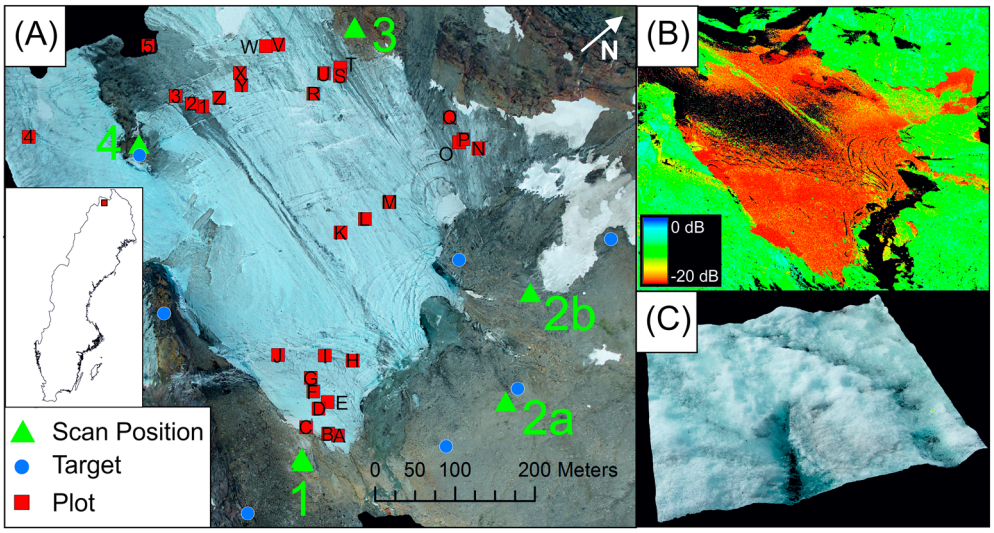

Figure 1. Study site. (a) Scan positions, targets, and plot locations overlaid onto an orthophotograph of lower Kårsaglaciären generated from glacier-scale SfM-MVS (not contemporaneous with plot surveys and used to generate an orthophotograph only). See Table S1 for plot descriptions. Note the location of Scan 2 varied slightly between the two surveys; (b) oblique viewpoint of TLS point cloud of the lower Kårsaglaciären rendered by return reflectance (dB) displaying areas of wet ice oblique to the TLS that exhibited low point density (in black); (c) example SfM-MVS plot dense point cloud viewed obliquely (Plot A, supraglacial channels, approximately 2 × 2 m).

this was reduced with lower point recovery on ice surfaces because of the lower reflectivity of ice at infrared wavelengths. The manufacturer-stated precision and accuracy is 0.005 m and 0.008 m, respectively [*RIEGL*, 2012]. A nominal spatial resolution of 0.1 m at 450 m range was applied resulting in an angular increment of 0.012°. At large ranges, the laser beam divergence (stated as 0.003 mm m^{-1}) is typically the largest source of error [*Carrivick et al.*, 2015] with beam widths of 0.015 m at 500 m range. The relative orientation of the surface would also have influenced the laser beam footprint through determining the angle of incidence.

Four TLS surveys of Kårsaglaciären were undertaken between 22 and 24 July 2013 from scan positions surrounding the ~1 km^2 lower glacier (Figure 1a). There was little overlap between the scans on the glacier ice itself, and so gaps in coverage resulted from occlusions behind obstacles or negligible returns from wet ice surfaces oblique to the TLS survey sites (Figure 1b). The first three scan positions were repeated after an interval of 3 days (25 and 26 July) to yield a second topographic model of the glacier. Accessibility and laser absorbance by snow precluded the acquisition of topographic data from the accumulation zone of the glacier. For survey control, a network of six tripod-mounted static targets was established surrounding the survey area utilizing bedrock outcrops and sites clearly visible throughout the survey area (Figure 1a). Using a minimum of four targets visible from each scan position, the TLS surveys were coregistered into a single local coordinate system. The standard deviations (or 3-D error) of the coregistrations were between 4.5 mm and 13.8 mm. The two merged scans of the lower glacier contained 15×10^6 and 9×10^6 points.

The open-source topographic point cloud analysis toolkit (ToPCAT) [*Brasington et al.*, 2012] was used to unify point densities and create two glacier DEMs. A DEM resolution of 2 m was specified, and cells containing fewer than four points were discarded (~20% of total cells). The mean cell elevation was applied to represent the glacier surface elevation, and the detrended standard deviation of elevations was used to represent subgrid roughness [*Vericat et al.*, 2014; *Smith and Vericat*, 2015]. The grids of the two DEMs were aligned to enable a DEM of Difference (DoD) to be calculated. The DoD represents changes on the glacier over a 3 day interval; however, the exact days over which this interval spans are not identical for each scan owing to different days of occupation.

3.2.2. Plot-Scale Topography From Structure From Motion Multi-View Stereo (SfM-MVS)

To characterize finer-scale topographic variability, 31 plots were surveyed using Structure from Motion Multi-View Stereo (SfM-MVS) photogrammetric techniques. The scale dependence of z_0 calculation is an important consideration [*Arnold and Rees*, 2003; *Fassnacht et al.*, 2009a]. *Rees and Arnold* [2006] observed two scale-free domains (<0.1 m and > ~1 m), suggesting that the intermediate region is characterized by a

definite scale. They suggest that topographic data of sampling interval of < 0.1 m and length of > 1 m with millimetric vertical accuracy is required to best represent z_0. Thus, plots were approximately 2 m × 2 m in size and 20 digital photographs of 6 megapixels were taken of each plot with a Canon PowerShot G11 digital SLR camera. Images surrounding each plot were taken from 2 m above ground with angular changes of $< 20°$ between adjacent camera locations to facilitate identification of correct keypoint correspondence [*Moreels and Perona*, 2007; *Bemis et al*., 2014]. Oblique convergent images were captured to avoid the doming effect observed when exclusively vertical images are used [*James and Robson*, 2014; *Smith and Vericat*, 2015]. Plots were distributed on the glacier surface to incorporate the greatest possible range of surface type and topographic variability and to ensure, as far as possible, good spatial coverage of the lower glacier surface (Figure 1a). Glacier surface types were classified into qualitative categories including smooth/superimposed ice, runnels, cryoconite, sun cups, blocky crystalline ice, supraglacial channels, dirty ice, light/medium/dense scree, shallow/deep crevasses, and snow (Table S1in the supporting information).

Groups of photographs pertaining to each plot were imported into Agisoft Photoscan Professional 1.1.6 and SfM algorithms implemented, to estimate simultaneously camera positions, camera intrinsic parameters, and scene geometry (see *James and Robson* [2012] and *Smith et al*. [2015] for further details). Georeferencing of the SfM point cloud was performed using control points surveyed with a TLS. Five reflective disk targets (50 mm diameter) were fixed into the ice in the plot corners and plot center and directed to face the nearest TLS scan position. The targets were identified in additional TLS surveys undertaken from each scan position that was focused on each plot. The 3-D coordinates of each target (referenced to the same local coordinate system as the TLS surveys) were imported and a linear similarity transformation performed to scale and georeference each SfM point cloud. Average georeferencing errors were subcentimeter (see supporting information Table S1). Using these coordinates, the intrinsic camera parameters and scene geometry were refined and the bundle adjustment rerun to optimize the image alignment by minimizing the sum of the reprojection error and the georeferencing error. Both original and optimized point clouds were calculated and MVS image-matching algorithms performed to produce final dense point clouds (Figure 1c). Average point density of the final plot point clouds was $>$300,000 points m^{-2}. ToPCAT was applied to the plot-scale SfM-MVS surveys for the generation of a DEM of 5 mm resolution. While TLS surveys of each plot were performed as part of the georeferencing, the absorbance of the near-infrared laser by ice and snow was such that relatively few TLS points were observed within each plot (typically 500 points m^{-2}), but this was sufficient to validate the SfM-MVS point clouds.

To analyze the temporal variability of ice surface roughness, of the 31 plots 9 were revisited after 3 days (Plots A–C, E, F, H, and S–V; Figure 1a). TLS targets were replaced and resurveyed as described above. Additionally, three of these nine plots (A, B, and F) were resurveyed again a few hours afterward.

To facilitate upscaling, the extent of each plot was mapped onto the glacier-scale TLS-derived DEM. Plot extents and DEM cells did not align perfectly owing to the variability of plot spacing, so the mean subgrid roughness value of all cells containing at least part of each plot was calculated to compare plot-scale and glacier-scale models. The DEM surveyed on the same day as the plot was used in each case.

3.2.3. Meteorological Data

Meteorological data were recorded during the survey interval to explain the surface-lowering rates observed. Air temperature was monitored every 30 min throughout the field campaign at an automatic weather station (AWS) located ~500 m down valley of the glacier terminus. The AWS comprised a Campbell Scientific CR200 data logger connected to air pressure, air temperature, relative humidity, wind speed, and wind direction sensors. This AWS has been in operation since 2007, and mean July temperatures have been 8.6°C, compared to −10.6°C in February.

3.3. Validation of Structure From Motion Multi-View Stereo Surveys

TLS data coincident and contemporaneous with each SfM-MVS plot survey were used to validate both nonoptimized and optimized SfM-MVS dense point clouds. Cloud-to-cloud comparisons were conducted in CloudCompare [*CloudCompare*, 2016]. The 3-D distance between each TLS point and its nearest neighbor in the dense SfM-MVS cloud was computed and split into *X*, *Y*, and *Z* components. Where either the *X* or *Y* components were $>$0.02 m, the validation point was discarded. The mean and median *Z* distances were calculated alongside the standard deviation and root-mean-square error (RMSE) for each plot. Beam divergence and laser footprint long axis were calculated [after *Schürch et al*., 2011] to estimate the error of

the TLS validation data. While only negligible differences between RMSE values for optimized and nonoptimized SfM-MVS point clouds were observed (typically ~ 1 mm), for each plot the point cloud with the lowest RMSE was used for analysis.

3.4. z_0 Calculation

Each plot-scale point cloud was rotated to be aligned with the prevailing wind direction, observed to be predominantly down glacier. Point clouds were cropped to ensure an approximately equal number of rows and columns. We undertook three different approaches, described in sequence below, to estimate z_0 from the microtopographic roughness data acquired. The first follows the method of *Munro* [1989] for the purposes of comparison with previous studies; the remaining two present new methods which utilize the greater volume of roughness information that can be gathered using raw and gridded TLS and SfM-MVS data sets. Differences between the three methods are summarized in Table 1.

3.4.1. Profile-Based Approach

To estimate z_0 following *Munro* [1989], we simplify the Lettau equation (1) by assuming that h^* can be represented by twice the standard deviation of elevations of the detrended profile ($2\sigma_d$, m), with the mean elevation set to 0 (Figure 2a) (similar to the "random roughness" metric commonly applied to soil and snow surfaces [e.g., *Kuipers*, 1957; *Fassnacht et al*., 2009a]). Roughness elements are modeled by calculating the number of upcrossings above the mean elevation (f) in any profile of length X (m). The frontal silhouette area of roughness elements in the profile is then estimated as

$$s = \frac{2\sigma_d X}{2f}, \tag{2}$$

and the ground area occupied by each roughness element (so-called lot area), S (m^2), is approximated as

$$S = \left(\frac{X}{f}\right)^2. \tag{3}$$

Thus, the aerodynamic roughness length for a given profile becomes

$$z_0 = \frac{f}{X}(\sigma_d)^2. \tag{4}$$

As demonstrated in Figure 2a, (4) makes the assumption of uniformly distributed roughness elements of equal height along the profile. Despite this, *Munro* [1989] found that it performed well as an approximation of z_0 differing by only 12% from the true z_0 value (though note the later reanalysis of *Andreas* [2002] which questioned height corrections to velocity profiles implemented by *Munro* [1989]). Using this method, z_0 was calculated for every profile ($n \approx 400$) in both orthogonal directions for each plot. Since profiles should be taken perpendicular to the wind direction, to avoid confusion, we state consistently wind direction when describing the z_0 value. Following normality tests, the probability distribution of profile-based z_0 values was characterized by the mean and standard deviation of values in each orthogonal direction.

3.4.2. DEM-Based Approach

Profile-based simplifications, while computationally efficient, discard large volumes of potentially useful topographic data. Such simplifications are more appropriate for the situation faced by *Munro* [1989] where, prior to the widespread application of TLS or SfM-MVS, limited manually measured point data were available (~30 points) and more demanding z_0 calculation methods cannot be supported. With a DEM-based approach, the following assumptions of the profile approach can be relaxed:

1. All roughness elements are of equal height.
2. All roughness elements are equally spaced.
3. No sheltering of roughness elements occurs.
4. The frontal area of roughness elements is equal for opposing wind directions (isotropy).

Considering the *Lettau* [1969] equation, a DEM-based approach enables the roughness frontal area s to be calculated directly (Figure 2b) for each cardinal wind direction, thereby relaxing assumptions (1), (2), and (4). Sheltering (assumption (3)) is implicitly represented by including only frontal areas above the detrended zero plane. Calculating the combined roughness frontal area across the plot, the planar plot area is then used as the ground area S (since the lot area per roughness element as specified by *Lettau* [1969] incorporates both

Table 1. Summary of z_0 Calculations

Quantity	Profile Based	DEM Based	Cloud Based
Drag coefficient		0.5	
Effective obstacle height h^* (m)	2 × detrended standard deviation of profile perpendicular to wind	Mean height of all points above the detrended plane	
Ground area S (m^2)	For each "roughness element" separately: $(X/f)^2$	Full plot planar area	Full plot 3-D surface area approximated by number of points after octree subsampling. No units
Silhouette area s (m^2)	Uniform roughness elements approximated. Frontal area of a "typical" roughness element calculated using equation (2) (see Figure 2a)	Exposed frontal area for each cardinal direction calculated across whole DEM. Only includes areas above detrended plane	Surface area facing each cardinal direction estimated by counting number of points with normal vector 45° either side of that direction. Only points above detrended plane where normal vector is <80° from horizontal. No units

the ground area of the roughness element and the surrounding plot area). Specifying the effective obstacle height h^* is more problematic, and the rationale for the use of $2\sigma_d$ by *Munro* [1989] is unclear. Considering assumption (3), only points that are above the detrended plane are considered and h^* is instead calculated as the mean deviation above this plane. Any single summary of obstacle height will be somewhat arbitrary; however, the mean deviation above this plane is perhaps most meaningful on an irregular ice surface. This DEM-based approach results in four z_0 values are generated for each plot, one for each cardinal direction.

3.4.3. Point Cloud-Based Approach

High-resolution surveying techniques produce dense point clouds containing rich information that require summary even for DEM construction. Using several simplifying assumptions, the dense point clouds were employed here directly, for a further method of z_0 calculation as follows.

Raw point clouds are not of a uniform density as the feature matching process as part of the SfM-MVS workflow may oversample more visible local topographic highs owing to their greater visibility in the raw images and higher density of successful matches [*Smith et al*., 2015]. To yield a uniform point density, the plot-scale point clouds were subsampled after detrending using an octree filter (a tree-based method of point cloud partitioning) [*Meagher*, 1982]. Normal vectors for each point were computed using triangulation (Figure 2 c), and the number of normal vectors facing each cardinal direction (i.e., within a 90° bin centered on the cardinal direction) was counted to represent s in each cardinal direction under the assumption that each point represents a comparable surface area following octree subsampling. Points below the detrended plane and "flat" surfaces defined as having a normal vector greater than 80° from horizontal were not used in the estimation of s. The plot area S was approximated by the total number of points in the cloud (approximating the 3-D surface area). Finally, the effective obstacle height was calculated as the mean height above the detrended plane of all points above that plane.

4. Results

4.1. Validation of Structure From Motion Multi-View Stereo

Quantitative comparison of SfM-MVS points with TLS survey points demonstrated good agreement between the two data sets. In four plots TLS surveys showed insufficient points for comparison with SfM-MVS owing to the poor reflectance of wet ice at the instrument wavelength. Across the remaining 27 plots for which validation data were available, the average mean absolute error (MAE) for nonoptimized point cloudes was 8.47 mm. Optimized SfM-MVS models performed slightly better (8.14 mm), though there was little observable difference between them (full details in Tables S1 and S2). However, MAE values were an order of magnitude below the mean of the estimated maximum error in the TLS points (69.66 mm) owing to the sometimes long survey ranges and beam divergence. Restricting analysis to situations where modeled TLS error was <10 mm, nonoptimized and optimized MAE values were 6.02 and 5.55 mm, respectively. Given the much shorter

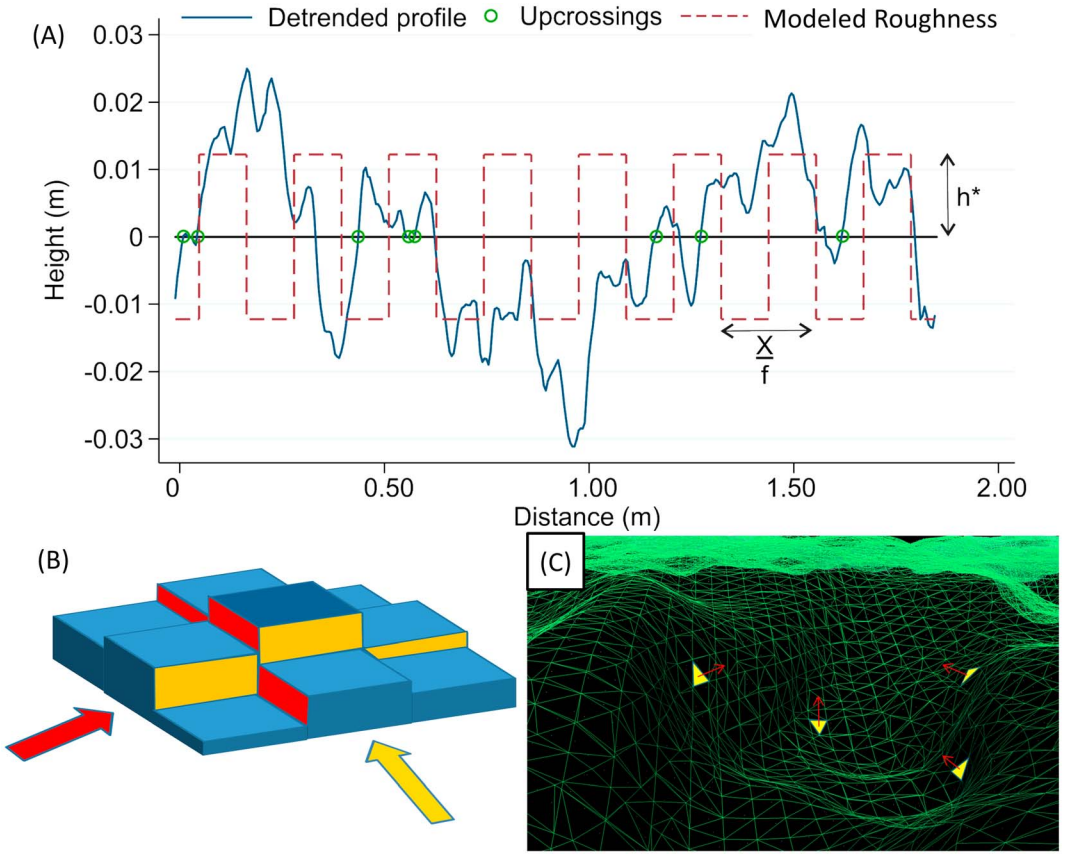

Figure 2. Schematic illustrations of z_0 calculations. (a) Conventional profile-based approach (shown for Plot N). Upcrossings are defined as points where the profile crosses the detrended mean moving from below the mean to above the mean. (b) DEM-based approach highlighting frontal area for two orthogonal wind directions. (c) Demonstration of normal vectors on a triangulated wireframe mesh of a point cloud (Plot N, for illustration only).

survey range for SfM-MVS than TLS, it is reasonable to assume that expected errors are lower from plot-scale SfM-MVS than for glacier-scale TLS and are millimeter scale [see *Smith and Vericat*, 2015].

4.2. Spatial Variability in Ice z_0

4.2.1. Comparison of z_0 Calculations

Table 2 shows the results for z_0 calculation from the three different methods. Using the concordance correlation [*Lin*, 1989, 2000] which measures agreement of variables rather than linearity, we found that when averaged in all directions, the strongest agreement was between DEM-based and point-cloud-based z_0 calculations ($\rho_c = 0.973$), with lower agreement between profile-based z_0 values and both DEM-based (0.730) and cloud-based (0.620) values. Separating the values into orthogonal components showed weaker agreement but a similar pattern (Figure S1). In general, point-cloud-based z_0 values were the highest (and had the lowest interquartile range) and DEM-based values the lowest, though differences between all three calculation methods were relatively minor with a range in overall average z_0 values of just 0.247 mm (Table 2).

4.2.2. Variability of z_0 Between Plots

A wide range of z_0 values was observed across the 31 plots on the ablation zone of Kårsaglaciären (Figure 3a). Summary statistics are separated out by direction in Table 2, and values for each plot are provided in Table S3. All z_0 values were > 0.05 mm, and the majority were < 3 mm. All plots containing deep crevasses and one containing shallow crevasses yielded values > 10 mm, comparable with those reported on very rough glacier ice [*Smeets et al.*, 1999]. Plots traversed by supraglacial channels exhibited consistently high z_0 values (>1 mm), while plots containing dirt cones on the ice surface also yielded locally high values. The presence of scree distributed over the ice surface also produces a high z_0 (~1 mm); however, the extent of debris cover is important with lower areal concentrations exhibiting a lower z_0 (particularly for the DEM-based approach).

Table 2. Summary of z_0 Values for All 31 Plots[a]

	Direction (Wind)						
z_0 Method	Up Glacier	Down Glacier	Glacier Flow-Parallel Average	True Left	True Right	Glacier Flow-Perpendicular Average	Overall Average
Profile							
Median (mm)			1.216			0.760	1.019
IQR (mm)			1.044			1.778	1.340
DEM							
Median (mm)	0.741	1.026	0.883	0.772	0.843	0.757	0.820
IQR (mm)	0.953	1.015	1.392	0.980	0.938	0.877	1.110
Point cloud							
Median (mm)	1.071	0.941	0.998	1.227	1.222	1.269	1.067
IQR (mm)	1.160	0.883	1.009	0.977	1.081	1.029	0.947

[a]The wind direction is given (i.e., wind blowing from "up glacier" or from the "true left," etc.). Thus, "glacier flow-parallel" profile-based values are for profiles orientated across the glacier surface (i.e., perpendicular to the wind direction). Robust metrics are provided owing to the nonnormality of the data set (see outliers in Figure 2a, right). IQR = interquartile range.

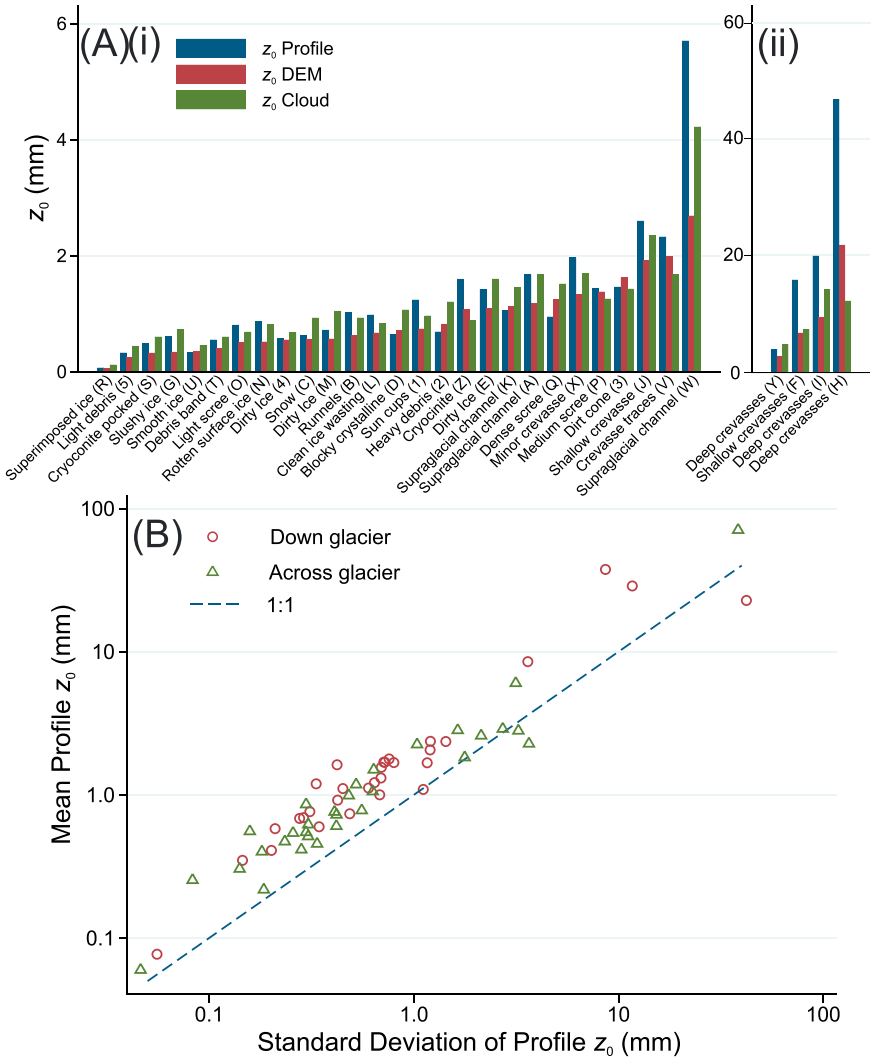

Figure 3. (a) Variability of z_0 between plot surfaces (ordered by z_0 DEM). See Table S3 for values. Plot IDs provided in parentheses (see Figure 1a for locations). Directionally averaged z_0 values are presented for each plot. (b) Relationship between mean and standard deviation of profile-based z_0 values presented separately for each orthogonal direction. Note log-log scale.

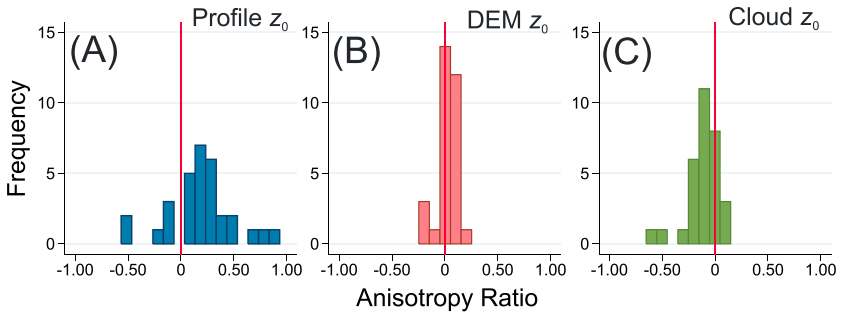

Figure 4. Summary of anisotropy ratio values for each method of z_0 calculation.

The lowest z_0 values were for surfaces classified as "smooth," "slushy," or "superimposed" ice (<0.3 mm). Intermediate values were observed for patches of snow cover, sun cups, runnels, and patches classified as "dirty ice" (with z_0 typically between 0.5 and 1 mm).

4.2.3. Variability of Profile Values Within a Plot

DEM and cloud-based methods generate a single value for the plot (for each cardinal direction), whereas extraction of profile-based z_0 values from a DEM enables multiple values to be compared for a single plot. Skewness-kurtosis tests confirmed normality of all sets of profiles; only one plot was not normal at $P < 0.01$, and all plots were normal at $P < 0.05$. With over 400 profile-based z_0 measurements in each direction per plot, analysis of the standard deviation of these values is informative (Figures 3b and S2). Mean values are consistently in line with DEM-based and cloud-based values; however, the variability about that mean is substantial. For two plots, the standard deviation of z_0 is greater than the mean. In all cases the high standard deviation of >20% of the mean z_0 value presents an important sampling issue for conventional topographic profiles.

4.2.4. Anisotropy

In Table 2, the largest differences between z_0 calculation methods emerge when the directionality of surface roughness is considered. Following *Smith et al*. [2006], an anisotropy ratio (Ω) is calculated for comparison of surface roughness in wind-parallel ($z_{0\parallel}$) and wind-perpendicular ($z_{0\perp}$) directions.

$$\Omega = \frac{z_{0\parallel} - z_{0\perp}}{z_{0\parallel} + z_{0\perp}}. \tag{5}$$

This ratio tends toward 1 when $z_{0\parallel}$ dominates, toward −1 when $z_{0\perp}$ dominates, and 0 when roughness is isotropic. Setting the down-glacier direction as parallel to the prevailing wind, Figure 4 summarizes the variation of anisotropy values between z_0 calculations. Profile-based metrics indicate greater z_0 for glacier flow-parallel winds and exhibit the largest range, DEM-based metrics suggest generally isotropic surfaces and have the smallest range of values, whereas cloud-based metrics highlight greater z_0 for winds blowing across the glacier. Detection of anisotropy thus appears to be an important discriminant of the metrics examined here.

A breakdown by plot is provided in Table S3 and Figure S3. The most extreme anisotropy ratio values (and the biggest differences between metrics) are observed in plots containing large surface features, such as crevasses or supraglacial channels. The specific values are sensitive to the orientation of the channel within the plot. However, no significant relationship was observed between anisotropy and z_0. The presence of debris often resulted in positive anisotropy ratios.

While profile-based approaches only separate orthogonal components, DEM-based analyses produced a z_0 value for each cardinal direction, and point-cloud-based metrics can yield a z_0 value for any given wind direction, though here, for comparability, only values for cardinal directions have been calculated. The difference between z_0 for two opposing wind directions is summarized as a percentage of the average z_0 value (for both directions). The DEM-based z_0 values exhibit greater variability for opposing wind directions (32% and 22% for glacier flow-parallel and glacier flow-perpendicular components, respectively) than cloud-based z_0 values (9% and 12%, respectively).

4.3. Modeling Surface Roughness at the Glacier Scale

Statistical relationships were explored between plot-scale z_0 and glacier-scale variables to provide a basis for upscaling z_0 beyond the plot (Figures 5a–5c). Large values of z_0 associated with crevasses had a significant

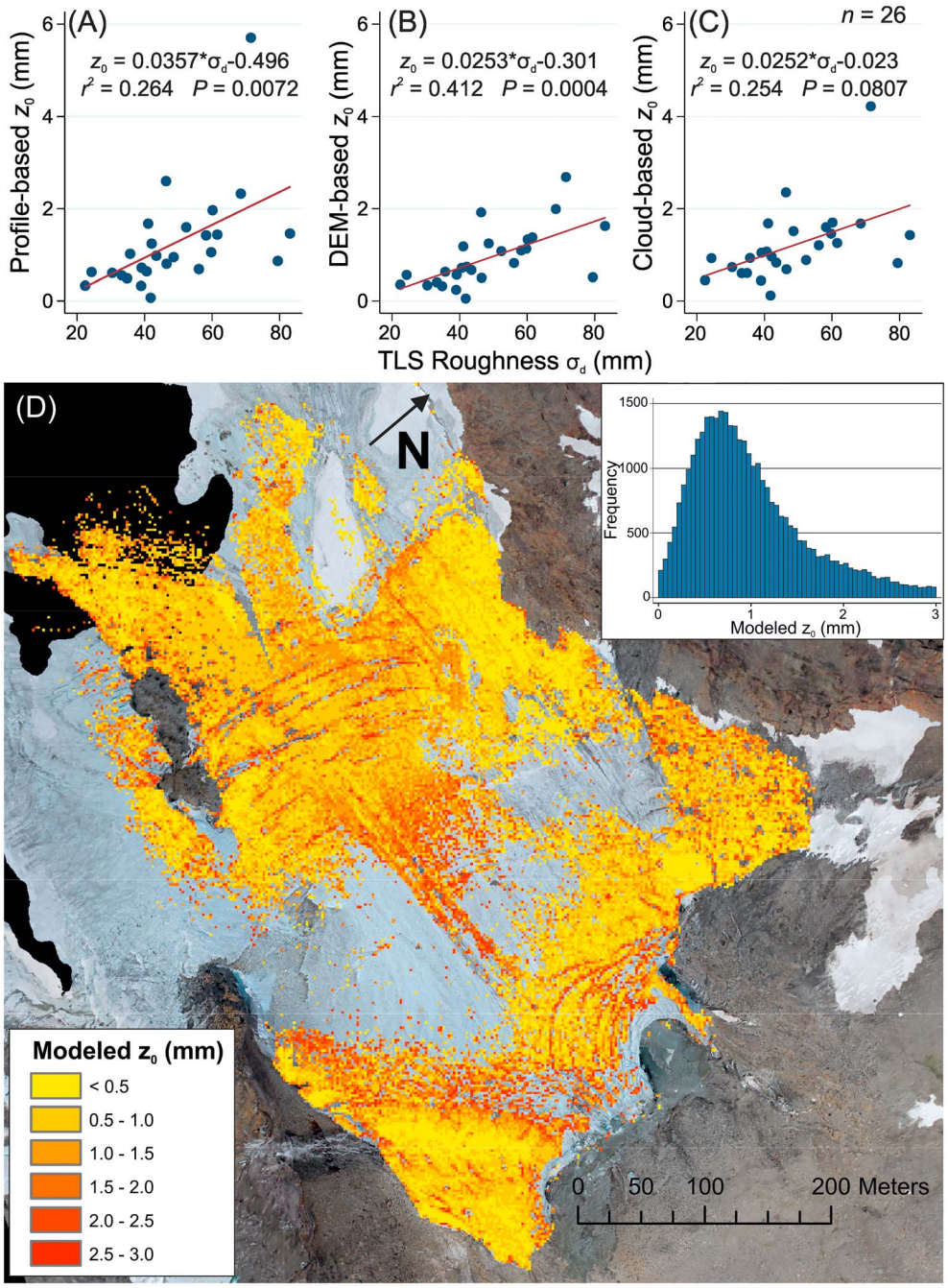

Figure 5. (a–c) Relationships between directionally averaged z_0 values and subgrid TLS roughness (represented by the detrended standard deviation of elevations). Model fits correspond to the regression parameters indicated (excludes Plots F, H, I, and Y). (d) Map of modeled glacier z_0 using TLS-derived subgrid roughness to upscale DEM-based z_0 (2 m resolution). Gaps relate to areas with insufficient TLS data to compute subgrid roughness or areas where predicted z_0 is $>$ 3 mm and beyond the range of the relationship demonstrated in Figure 5b. The distribution of modeled z_0 values is shown (inset).

leverage over such statistical relationships. Thus, the four plots that comprise Figure 3a-ii were excluded from upscaling analysis [*Helsel and Hirsch*, 1992]. A further plot, located in the accumulation area, was excluded as there were insufficient coincident TLS data.

No statistically significant relationships were observed between z_0 and plot mean elevation, plot distance from glacier terminus, or plot mean slope. However, a significant relationship was observed between subgrid TLS roughness and all three z_0 values; the relationship was strongest for DEM-based z_0 values (Figure 5b). This

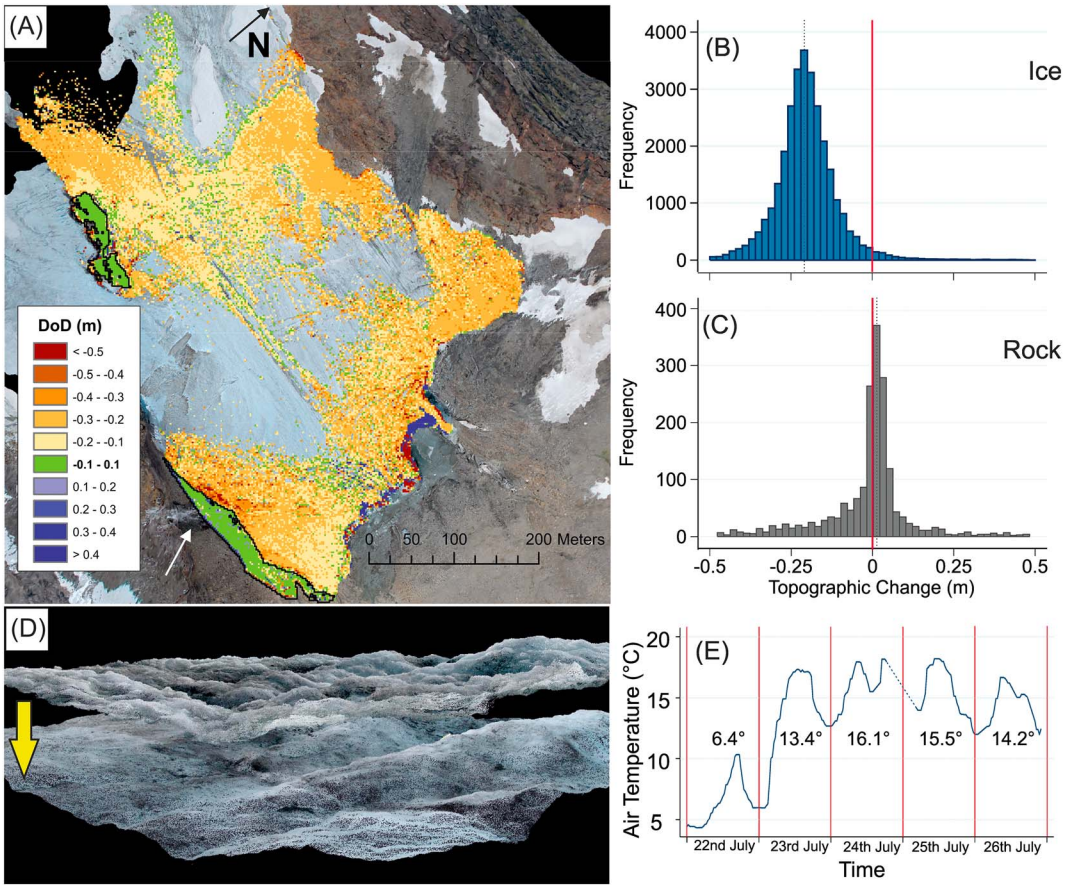

Figure 6. (a) DEM of difference from repeat TLS over a 3 day interval. Bedrock areas are outlined in black. The waterfall supplying a subglacial stream is indicated with a white arrow. Frequency histogram of observed topographic changes (b) for ice surfaces and (c) for rock and proglacial debris surfaces. Only changes ±0.5 m shown for clarity. (d) Example of lowering observed from repeat SfM-MVS dense point clouds ("Dirty Ice" Plot E over a 3 day interval showing an average surface elevation change of 0.23 m); (e) 30 min smoothed temperature data recorded at the AWS over the survey interval. Mean daily temperatures reported for each day. A data gap spanning 24 and 25 July has been interpolated (dashed line).

relationship presented the possibility of upscaling z_0 estimates beyond the plot to represent z_0 variability over the majority of the lower glacier (where data are available), though since differences in absolute z_0 values between methods were smaller than the natural variability of z_0 on a single glacier, all three calculation methods are likely to be equally suitable in this regard. The relationship for DEM-based z_0 values was used to provide such a glacier-scale z_0 map in Figure 5d using the first TLS survey as a basis for upscaling. As plot data were only reliable where $z_0 < 3$ mm, only cells in this range were included.

Across the glacier, areas of relatively high z_0 values were found to be associated with crevasse features (Figure 5d) and the medial moraine running through the center of the glacier. Considering only the 0.14 km^2 area of the ablation area of Kårsaglaciären for which sufficient TLS data were available to estimate z_0, the mean modeled z_0 was 0.99 mm, the median value was 0.85 mm, and the standard deviation was 0.61 mm. This is likely to be an underestimate of z_0 as some notable areas of high subgrid roughness were not able to be included (e.g., close to the glacier terminus).

4.4. Temporal Changes in z_0

4.4.1. Glacier-Scale Changes

Over the 3 day TLS survey interval, a substantial amount of ice surface lowering was observed throughout the ablation zone (Figure 6a). To demonstrate that the observed lowering is not a survey artifact, the change detected in two bedrock areas was compared with that seen on the ice surface (Figures 6b and 6c). The two distributions are statistically different. Median change observed by TLS over bedrock was 7.28 mm (over

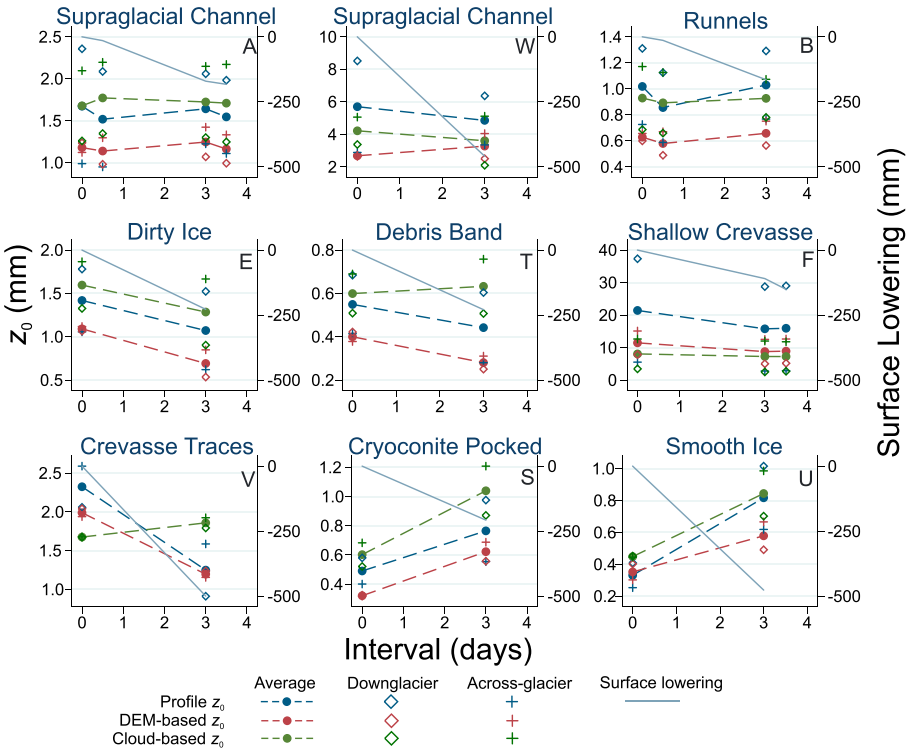

Figure 7. Plot-scale changes in z_0 values with surface lowering over several days of intense melting (Figure 6e). Note different scales on z_0 axes for improved clarity of changes within each plot. Plot IDs are indicated in the top right corner of each panel and relate to Figure 1a. Survey intervals were not exactly contemporaneous with the DoD in Figure 6a.

7,532 m^2 outlined in bold in Figure 6a), whereas that observed on ice surfaces was −206.99 mm (over 0.12 km^2). At higher elevations within the survey area, surface lowering rates (~150 mm) are slightly less than at the glacier margins and across the lower parts of the glacier (~200 mm). Relatively high rates of lowering (~280 mm) were observed on the true right of the glacier which corresponds to the entry point of a stream running under the ice along the glacier margin, fed by a waterfall indicated in the lower left of Figure 6a. A large area at the true left margin of the glacier close to the south facing bedrock outcrop also showed higher than average lowering (~250–300 mm). Large elevation changes (>2 m) were also observed at the terminus where Kårsaglaciären calves into a small proglacial lake. Glacier advances and calving events can be clearly observed from the DoD at the terminus (Figure 6a) and represent the biggest elevation changes over the 3 day survey interval.

4.4.2. Plot-Scale Changes

The change in z_0 observed over the nine resurveyed plots is summarized in Figure 7. Plots were resurveyed after an interval of 0.5, 3, and/or 3.5 days resulting in a maximum of four time periods for a single plot. Values for all three z_0 calculation metrics are presented, incorporating averaged values for all directions and values separated into both down-glacier and across-glacier averages. Analysis of the AWS record revealed that the period following 23 July 2013 (Figure 6e) was considerably warmer than any time previously in the melt season of 2013 when average daily temperatures rarely rose above 10°C.

Despite high rates of surface lowering (e.g., Figure 6d), estimated z_0 values (Figure 7) remained relatively constant for three plots containing surface meltwater features (supraglacial channels or runnels). Decreases in z_0 were observed for plots where surface debris was observed (dirty ice or debris band) or which contained minor stress features (a shallow crevasse or crevasse traces), while increases in z_0 were observed where the ice was very smooth and on a plot pocked with cryoconite. All three z_0 values were well correlated, and, as reported in section 4.2.1, point-cloud-based z_0 values were typically highest while profile-based z_0 values had the highest variability.

Over 3 days, observed surface lowering was typically ~0.2 m; however, three plots exhibited much higher values >0.45 m. These rapidly lowering plots covered a wide range of z_0 values, including the more deeply

incised of the two supraglacial channels and crevasse traces and smooth ice, all of which were located in the upper ablation zone toward the true left margin of the glacier. Overall, observed surface lowering was positively correlated with degree days ($r = 0.87$, $n = 24$, $P < 0.0001$). The three rapidly lowering plots experienced surface lowering rates between 10.2 and 11.1 mm K^{-1} day^{-1}, while other plots were between 4.2 and 7.0 mm K^{-1} day^{-1}.

5. Discussion

5.1. Methods for Calculating z_0 From Topographic Data

Previously, collection of topographic data suitable for z_0 calculation required either laborious and time-consuming measurement or the construction of bespoke equipment [e.g., *Herzfeld et al*., 2000]. Recent advances in the acquisition of high-resolution topography have revolutionized the study of Earth surface processes [*Passalacqua et al*., 2015], yet the calculation of z_0 from ice surface topography has typically retained assumptions put in place under conditions of limited topographic data and computational power. With these restrictions lifted, the DEM-based analysis presented herein permits frontal area exposed to a prevailing wind direction to be calculated explicitly over an ice (or snow) surface. Furthermore, with alternative approximations, z_0 can be rapidly estimated directly from point clouds.

Overall differences among profile, raster, and cloud-based z_0 measurements were relatively minor (Table 2). More detailed comparison of calculation methods reveals three weaknesses in the conventional topographic profile-based approach. First, calculating z_0 from a single topographic profile presents a sampling issue given the variability of topographic profile-based values within a single plot (Figure 3b). Similar z_0 variability was also reported by *Irvine-Fynn et al*. [2014]. Second, while orthogonal profiles are often computed, the different frontal areas from two opposing wind directions cannot be resolved. DEM-based z_0 values for opposing wind directions differed by $> 20\%$ meaning conventional approaches may not be appropriate for anisotropic surfaces. Third, topographic profile-based z_0 values do not account for sheltering of an obstacle. With many ice surface features streamlined by either wind or water flows having continuous topographic expressions for tens of meters or more (sastrugi, for example [*Jackson and Carroll*, 1978]), such an assumption is limiting for glacier surfaces. This important weakness is revealed when z_0 values are separated into orthogonal directions (Figure 4).

In the extreme case where a crevasse or supraglacial channel is aligned perpendicular to the prevailing wind direction (Figure 8a) a detrended topographic profile will not detect this feature even if located within the crevasse or channel and would yield a relatively low z_0 value. Conversely, if the plot were rotated by 90° (Figure 8b), a detrended topographic profile perpendicular to the wind direction would yield a relatively high z_0 value. However, visual examination of the two plot surfaces in Figure 8 reveals that the plot in Figure 8a has a greater frontal area exposed to the prevailing wind, whereas the plot in Figure 8b is relatively streamlined to the wind direction. In this case computing z_0 using frontal area calculated from a DEM or approximated from a point cloud results in a higher z_0 for Plot 8A, the opposite of profile-based z_0 values. Such differences are not seen when uniform arrays of discrete roughness elements are present (from which the *Lettau* [1969] equation was derived) and are only significant where natural streamlined surfaces are the focus of study.

5.2. Spatial Variability of z_0 and Potential for Upscaling

A wide range of z_0 values for ice surfaces is reported in the literature; yet in this study a similar range of z_0 values was observed over a single glacier ablation area. Our mean z_0 value of ~ 1 mm reflects the typical values reported in the literature [*Brock et al*., 2006]. Indeed, the "typical" ice roughness value of 0.66 mm that is applied in the glacier-scale distributed surface energy balance model of *Arnold et al*. [2006] is similar to our median modeled value of 0.85 mm (Figure 5d). However, considering DEM-based z_0 values in this study, variation over 3 orders of magnitude was detected from 0.05 mm on superimposed ice to 22 mm for a deep crevasse. It is clear that a single z_0 value cannot accurately represent the important contribution of z_0 to glacier melt. Prominent surface features (e.g., crevasses) result in locally high z_0 values. Scale dependency of z_0 values requires further investigation; however, the sampling method used here captures the length scales identified by *Rees and Arnold* [2006].

The significance of the relationship between z_0 calculated from plot-scale SfM-MVS and glacier-scale TLS roughness suggests that the relevant components of topographic variability influencing z_0 can be approximated at the

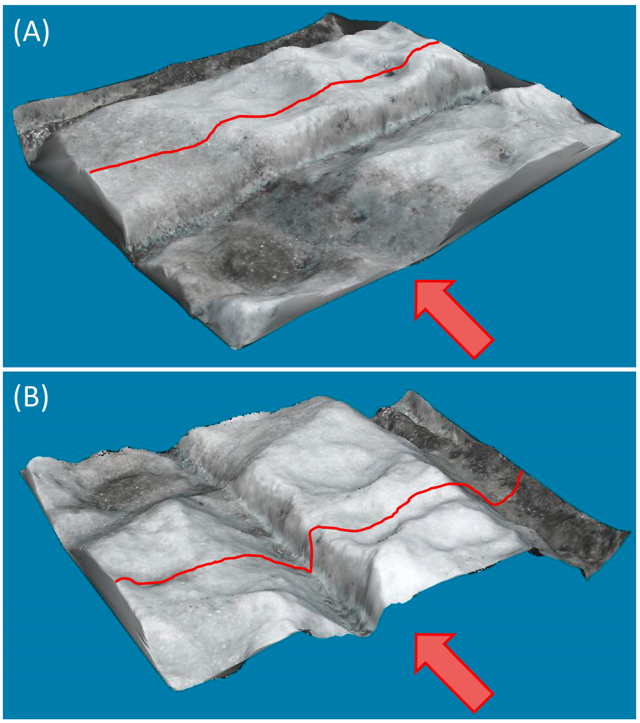

Figure 8. Demonstration of differences between z_0 anisotropy ratios for different calculation methods. The plot surface in Figure 8a is rotated through 90° in Figure 8b, while the prevailing wind direction remains constant. (a) A greater frontal area is exposed to the prevailing wind; however, (b) a profile perpendicular to the wind direction shows greater topographic variability.

glacier scale. The modeled z_0 map presented in Figure 5d contains substantial data gaps, though these could be filled with a dense network of survey stations. However, caution is required since approximation of z_0 with a simple metric of subgrid roughness is a considerable simplification and does not capture the directional variability observed with the more sophisticated metrics we investigated at the plot scale. Nevertheless, the relationships in Figure 5 suggest that a reasonable approximation of glacier-scale z_0 variability can be made using topographic data products that are increasingly available. Indeed, with the increased ease of data acquisition, upscaling z_0 to represent the variability over the glacier scale becomes a distinct possibility. Existing large-scale TLS [e.g., *Kerr et al.*, 2009; *Nield et al.*, 2012] and SfM-MVS [e.g., *Immerzeel et al.*, 2014; *Ryan et al.*, 2015] survey campaigns demonstrate this enhanced capability clearly.

Glacier surface energy balance calculations require estimates of turbulent fluxes of sensible and latent heat, and these are typically derived from high-resolution meteorological observations alongside a single z_0 value to represent the ice surface [e.g., *Arnold et al.*, 2006]. However, as this study has shown, an assumption of homogeneous z_0 values over entire glacier surfaces is questionable. Derivation of a distributed z_0 map such as is presented in Figure 5d therefore opens up several key possibilities for those interested in modeling glacier surface energy balance. First, it allows the modeler to compare z_0 acquired at a point with a range of values across a whole glacier and thus assess how representative it is. Second, it permits analyses of scale dependence. Since velocity profile measurements of z_0 reflect not just the surface in the immediate vicinity of the velocity profile but are the aggregate effect of surface obstacles distributed over a larger fetch area, a z_0 value for a single 4 m^2 cell in Figure 5d cannot be directly compared with velocity-profile-derived z_0 values at that same point. Rather, aggregation of heterogeneous z_0 values over areas representing an estimated fetch of the wind enables comparison with wind-profile-derived values [*Panofsky*, 1984]. The distributed nature of z_0 in Figure 5d will also assist with future calculations of varying z_0 values with varying wind direction. Finally, given that many inputs to surface energy balance models are gridded data sets, the inclusion of a dynamic and distributed z_0 map, rather than a single assumed value, is a logical next step.

5.3. Temporal Variability of z_0

Our observations of temporal variability in ice surface roughness with surface melt were acquired on Kårsaglaciären during a short period of relatively high air temperatures and agree with previously reported findings [e.g., *Brock et al.*, 2000, 2006; *Smeets and van den Broeke*, 2008]. Ice with surface debris or small amounts of dirt on the surface tended to become smoother, as did surfaces exhibiting small crevasse features suggesting preferential melting out of protruding roughness. Supraglacial channels did not exhibit such a decline in roughness possibly as down cutting kept pace with preferential melting. This variable response contrasts with the systematic increase in roughness observed on melting snow surfaces [*Fassnacht et al.*, 2009b].

Substantial surface melt was recorded over just 4 days (Figures 6 and 7). Average surface lowering was 0.2 m and showed a similar association between surface lowering rates and degree days as reported for Norwegian glaciers by *Laumann and Reeh* [1993] (5.5–7.5 mm K^{-1} day^{-1}), and rates are similar to the maximum values reported in *Wallén* [1948]. Three plots showed substantially higher surface lowering rates; these could not be discriminated by surface roughness or other features and instead appeared to reflect variation in incoming radiation being relatively flat plots positioned close to a south facing slope. Although surface lowering rates were rapid, the monitoring interval of just 4 days is insufficient to quantify the full range of ice roughness variability through the melt season. With a longer monitoring period over seasonal timescales, a wider range of roughness values is likely to be observed.

5.4. Further Work

The alternative z_0 calculation methods introduced here require validation using velocity profile or eddy correlation data [*Nield et al.*, 2013]. Similarly, modeled z_0 variability at the glacier scale requires validation both through finer scale measurements and through incorporation into spatially distributed surface energy balance models that are in turn validated against proglacial stream discharge measurements. Velocity profile data are needed alongside the distributed z_0 map of Figure 5d and map of glacier surface change in Figure 6a to validate the novel approach of z_0 estimation outlined herein and to examine the relevant scales at which to aggregate microtopography-derived z_0 estimates. With glacier-scale topography acquired through TLS or SfM-MVS, distributed energy balance models have the potential to incorporate sophisticated models of insolation by calculating shading from valley topography directly. Orthophotograph mosaics are a further output of plot-scale SfM-MVS that could be used to estimate surface albedo directly [*Dumont et al.*, 2011; *Rippin et al.*, 2015]. In addition, glacier-scale surveys may be able to bridge the gap between microtopography and satellite remote sensing of glacier surfaces for a more extensive upscaling of z_0 as demonstrated by *Blumberg and Greeley* [1993] and investigated on glacier surfaces by *Rees and Arnold* [2006].

Conventional methods of estimating z_0 from topographic profiles make several assumptions about the nature of the surface which is typically simplified as a regular array of uniform roughness elements (e.g., Figure 2a). Here we have presented a novel method of calculating z_0 directly from high-resolution DEMs that does not rely upon such simplifying assumptions. However, further investigation as to the specific parameters used in z_0 calculation (detailed in Table 1) is required, particularly the representation of effective obstacle height.

Sheltering of surfaces has been studied in detail in the atmospheric sciences and in investigations of aeolian erosion [e.g., *Garratt*, 1992; *Bottema*, 1996; *Chappell and Heritage*, 2007]. While *Garratt* [1992] suggested a displacement height of 0.7 h^* for most natural surfaces, the assumption made in Table 1 (for DEM-based and cloud-based z_0 calculations) was that frontal areas below the detrended plane level would be effectively sheltered. For the ice surfaces investigated herein, roughness element density (i.e., frontal area divided by surface area [*Wooding et al.*, 1973]) was <0.13 in all plots aside from one deeply crevassed plot and thus still within the range for which the *Lettau* [1969] equation holds. Certainly, more sophisticated sheltering parameterizations should be investigated [see *Raupach*, 1992; *Chappell et al.*, 2010] and the availability of high-resolution topographic data facilitates more direct inclusion of mutual sheltering of roughness elements [see *Smith*, 2014]. Similarly, the average drag coefficient of 0.5 used here is likely to be an overestimate for many glacier surfaces which tend to be streamlined [*Wieringa*, 1993; *Smeets et al.*, 1999] in at least one direction and would thus exhibit a much lower drag coefficient [*Powell*, 2014]. As demonstrated in Figure 8, the degree of streamlining and hence the drag coefficient may be dependent on the wind direction.

6. Conclusions

Through direct representation of the surface area of roughness elements, more sophisticated parameterizations of z_0 from ice surface topography can be realized from high-resolution three-dimensional survey data. Properties of surface roughness that best represent the process of momentum transfer from air flows to the ice surface can be quantified directly, enabling calculation of z_0 from topographic data to better reflect the underlying theoretical equations. When averaged over all cardinal wind directions, there is little difference between the novel DEM-based z_0 values and values calculated from profiles using assumptions on the form

of surface roughness. However, large differences emerge when z_0 is calculated separately for each wind direction, particularly where surface roughness is anisotropic.

The aerodynamic roughness of ice surfaces can be estimated at the glacier scale using a relationship established between z_0 and subgrid roughness of topographic models gridding at the meter scale. Such upscaling is important considering (i) the wide variability of z_0 over 3 orders of magnitude over a relatively small glacier ablation zone; (ii) the lack of a statistical relationship between z_0 and more general topographic variables such as elevation and slope; and (iii) the relatively large effect that z_0 variability has on estimations of turbulent heat fluxes and glacier ice melt, particularly in the context of future climate warming. With increased availability of high-resolution topographic data at the glacier scale, surface energy balance models can incorporate distributed z_0 parameterizations and better predict rates of ice loss under climate change scenarios.

Acknowledgments
Fieldwork was funded by EU INTERACT grants awarded to Bingham (LARGE) and Rippin (SAGLA) and a grant from the Carnegie Trust for the Universities of Scotland awarded to Bingham. We gratefully thank the Abisko Scientific Research Station (ANS) for hospitality and logistical support and Kallax Flyg for helicopter support.

References

Ahlmann, H. W., and O. Tryselius (1929), Der Kårsa-Gletscher in Schwedisch-Lappland, *Geogr. Ann.*, *11*, 1–32.
Andreas, E. L. (2002), Parameterizing scalar transfer over snow and ice: A review, *J. Hydrometeorol.*, *3*(4), 417–432.
Andreas, E. L. (2011), A relationship between the aerodynamic and physical roughness of winter sea ice, *Q. J. R. Meteorol. Soc.*, *137*, 1581–1588.
Arnold, N. S., and W. G. Rees (2003), Self-similarity in glacier surface characteristics, *J. Glaciol.*, *49*(167), 547–554.
Arnold, N. S., W. G. Rees, A. J. Hodson, and J. Kohler (2006), Topographic controls on the surface energy balance of a high Arctic valley glacier, *J. Geophys. Res.*, *111*, F02011, doi:10.1029/2005JF000426.
Bagnold, R. A. (1941), *The Physics of Wind-Blown Sand and Desert Dunes*, pp. 265, Methuen, London.
Banke, E. G., and S. D. Smith (1973), Wind stress on Arctic sea ice, *J. Geophys. Res.*, *78*, 7871–7883, doi:10.1029/JC078i033p07871.
Bemis, S. P., S. Micklethwaite, D. Turner, M. R. James, S. Akciz, S. T. Thiele, and H. A. Bangash (2014), Ground-based and UAV-Based photogrammetry: A multi-scale, high-resolution mapping tool for structural geology and paleoseismology, *J. Struct. Geol.*, *69*, 163–178.
Bintanja, R., and M. R. van den Broeke (1994), Local climate, circulation and surface-energy balance of an Antarctic blue-ice area, *Ann. Glaciol.*, *20*, 160–168.
Bintanja, R., and M. R. van den Broeke (1995), The surface energy balance of Antarctic snow and blue ice, *J. Appl. Meteorol.*, *34*(4), 902–926.
Blumberg, D. G., and R. Greeley (1993), Field studies of aerodynamic roughness length, *J. Arid Environ.*, *25*, 39–48.
Bodin, A. (1993), Physical properties of the Kårsa glacier, Swedish Lapland, Stockholm, University of Stockholm, Department of Physical Geography, Research Report 17.
Bottema, M. (1996), Roughness parameters over regular rough surfaces: Experimental requirements and model validation, *J. Wind Eng. Ind. Aerodyn.*, *64*, 249–265.
Braithwaite, R. J., and O. B. Olesen (1990), Response of the energy balance on the margin of the Greenland ice sheet to temperature changes, *J. Glaciol.*, *36*, 217–21.
Brasington, J., D. Vericat, and I. Rychkov (2012), Modelling river bed morphology, roughness and surface sedimentology using high resolution terrestrial laser scanning, *Water Resour. Res.*, *48*, W11519, doi:10.1029/2012WR012223.
Brock, B. W., I. C. Willis, M. J. Sharp, and N. S. Arnold (2000), Modelling seasonal and spatial variations in the surface energy balance of Haut Glacier d'Arolla, Switzerland, *Ann. Glaciol.*, *31*, 53–62.
Brock, B. W., I. C. Willis, and M. J. Sharp (2006), Measurement and parameterization of aerodynamic roughness length variations at Haut Glacier d'Arolla, Switzerland, *J. Glaciol.*, *52*, 281–297.
Brock, B. W., C. Mihalcea, M. P. Kirkbride, G. Diolaiuti, M. E. J. Cutler, and C. Smiraglia (2010), Meteorology and surface energy fluxes in the 2005–2007 ablation seasons at the Miage debris-covered glacier, Mont Blanc Massif, Italian Alps, *J. Geophys. Res.*, *115*, D09106, doi:10.1029/2009JD013224.
Carrivick, J. L., M. W. Smith, and D. M. Carrivick (2015), High-resolution topography of the upper Tarfala valley, *GFF*, 1–14.
Chappell, A., and G. L. Heritage (2007), Using illumination and shadow to model aerodynamic resistance and flow separation: An isotropic study, *Atmos. Environ.*, *41*, 5817–5830.
Chappell, A., S. Van Pelt, T. Zobeck, and Z. Dong (2010), Estimating aerodynamic resistance of rough surfaces using angular reflectance, *Remote Sens. Environ.*, *114*, 1462–1470.
CloudCompare (2016), CloudCompare version 2.6.1, GPL software. [Available at http://www.cloudcompare.org/.]
Counihan, J. (1971), Wind tunnel determination of the roughness length as a function of the fetch and the roughness density of three-dimensional roughness elements, *Atmos. Environ.*, *5*, 637–642.
Denby, B., and W. Greuell (2000), The use of bulk and profile methods for determining surface heat fluxes in the presence of glacier winds, *J. Glaciol.*, *46*(154), 445–452.
Denby, B., and P. Smeets (2000), Derivation of turbulent flux profiles and roughness lengths from katabatic flow dynamics, *J. Appl. Meteorol.*, *39*(9), 1601–1612.
Dong, Z., X. Lui, and X. Wang (2002), Aerodynamic roughness of gravel surfaces, *Geomorphology*, *43*, 17–31.
Dumont, M., P. Sirguey, Y. Arnaud, and D. Six (2011), Monitoring spatial and temporal variations of surface albedo on Saint Sorlin Glacier (French Alps) using terrestrial photography, *Cryosphere*, *5*(3), 759–771.
Fassnacht, S. R., J. D. Stednick, J. S. Deems, and M. V. Corrao (2009a), Metrics for assessing snow surface roughness from digital imagery, *Water Resour. Res.*, *45*, W00D31, doi:10.1029/2008WR006986.
Fassnacht, S. R., M. W. Williams, and M. V. Corrao (2009b), Changes in the surface roughness of snow from millimetre to metre scales, *Ecol. Complex.*, *6*, 221–229.
Fryrear, D. W. (1985), Soil cover and wind erosion, *Trans. ASAE*, *28*, 781–784.
Garratt, J. R. (1992), *The Atmospheric Boundary Layer*, *Cambridge Atmospheric and Space Sci. Ser.*, pp. 336, Cambridge Univ. Press, Cambridge, U. K.
Giesen, R. H., L. M. Andreassen, J. Oerlemans, and M. R. Van Den Broeke (2014), Surface energy balance in the ablation zone of Langfjordjøkelen, an arctic, maritime glacier in northern Norway, *J. Glaciol.*, *60*(219), 57–70.
Greuell, W., and C. Genthon (2004), Modelling land-ice surface mass balance, in *Mass Balance of the Cryosphere: Observations and Modelling of Contemporary and Future Changes*, pp. 117–168, Cambridge Univ. Press, Cambridge, U. K.

Greuell, W., and P. Smeets (2001), Variations with elevation in the surface energy balance on the Pasterze (Austria), *J. Geophys. Res.*, *106*(D23), 31,717–31,727, doi:10.1029/2001JD900127.
Hay, J. E., and B. B. Fitzharris (1988), The synoptic climatology of ablation on a New Zealand glacier, *J. Clim.*, *8*, 201–215.
Helsel, D. R., and R. M. Hirsch (1992), *Statistical Methods in Water Resources*, Springer-Verlag, New York.
Herzfeld, U. C., H. Mayer, W. Feller, and M. Mimler (2000), Geostatistical analysis of glacier-roughness data, *Ann. Glaciol.*, *30*, 235–242.
Hock, R. (2005), Glacier melt: A review of processes and their modelling, *Prog. Phys. Geogr.*, *29*(3), 362–391.
Hock, R., and B. Holmgren (1996), Some aspects of energy balance and ablation of Storglaciären, northern Sweden, *Geogr. Ann.*, *78A*(2–3), 121–131.
Hock, R., and B. Holmgren (2005), A distributed surface energy-balance model for complex topography and its application to Storglaciären, Sweden, *J. Glaciol.*, *51*(172), 25–36.
Holmgren, B. (1971), *Climate and Energy Exchange on a Sub-polar Ice Cap in Summer. Arctic Institute of North America Devon Island Expedition 1961–1963*, Uppsala, Uppsala Universitet, Meteorologiska Institutionen, Meddelande 111.
Immerzeel, W. W., P. D. A. Kraaijenbrink, J. M. Shea, A. B. Shrestha, F. Pellicciotti, M. F. P. Bierkens, and S. M. de Jong (2014), High-resolution monitoring of Himalayan glacier dynamics using unmanned aerial vehicles, *Remote Sens. Environ.*, *150*, 93–103.
Irvine-Fynn, T. D. L., E. Sanz-Ablanedo, N. Rutter, M. W. Smith, and J. H. Chandler (2014), Measuring glacier surface roughness using plot-scale, close-range digital photogrammetry, *J. Glaciol.*, *60*, 957–969.
Ishikawa, N., I. F. Owens, and A. P. Sturman (1992), Heat balance characteristics during fine periods on the lower parts of the Franz Josef Glacier, South Westland, New Zealand, *Int. J. Climatol.*, *12*(4), 397–410.
Jackson, B. S., and J. J. Carroll (1978), Aerodynamic roughness as a function of wind direction over asymmetric surface elements, *Boundary Layer Meteorol.*, *14*, 323–330.
James, M. R., and S. Robson (2012), Straightforward reconstruction of 3D surfaces and topography with a camera: Accuracy and geoscience application, *J. Geophys. Res.*, *117*, F03017, doi:10.1029/2011JF002289.
James, M. R., and S. Robson (2014), Mitigating systematic error in topographic models derived from UAV and ground-based image networks, *Earth Surf. Processes Landforms*, *39*, 1413–1420, doi:10.1002/esp.3609.
Karlén, W. (1973), Holocene glacier and climatic variations, Kebnekaise Mountains, Swedish Lapland, *Geogr. Ann.*, *55A*(1), 29–63.
Kerr, T., I. Owens, W. Rack, and R. Gardner (2009), Using ground-based laser scanning to monitor surface change on the Rolleston Glacier, New Zealand, *J. Hydrol.*, *48*, 59–71.
Kuipers, H. (1957), A reliefmeter for soil cultivation studies, *Neth. J. Agric. Sci.*, *5*, 255–267.
Laumann, T., and N. Reeh (1993), Sensitivity to climate change of the mass balance of glaciers in southern Norway, *J. Glaciol.*, *39*, 656–665.
Lettau, H. H. (1969), Note on aerodynamic roughness parameter estimation on the basis of roughness element description, *J. Appl. Meteorol.*, *8*, 828–832.
Lin, L. I. -K. (2000), A note on the concordance correlation coefficient, *Biometrics*, *56*, 324–325.
Lin, L. I.-K. (1989), A concordance correlation coefficient to evaluate reproducibility, *Biometrics*, *45*, 255–268.
MacKinnon, D. J., G. D. Clow, R. K. Tigges, R. L. Reynolds, and P. S. Chavez (2004), Comparison of aerodynamically and model-derived roughness lengths (z_0) over diverse surfaces, central Mojave Desert, California, USA, *Geomorphology*, *63*(1), 103–113.
Marcus, M. G., R. D. Moore, and I. F. Owens (1984), Short-term estimates of surface energy transfers and ablation on the lower Franz Josef Glacier, South Westland New Zealand, *N. Z. J. Geol. Geophys.*, *28*, 559–67.
Meagher, D. (1982), Geometric modelling using octree encoding, *Comput. Graphics Image Process.*, *19*, 129–147.
Millikan, C. M. (1938), A critical discussion of turbulent flows in channels and circular tubes, in *Proceedings of the 5th International Congress on Applied Mechanics Cambridge, MA*, pp. 386–392, Wiley/Chapman and Hall, New York.
Moreels, P., and P. Perona (2007), Evaluation of features detectors and descriptors based on 3D objects, *Int. J. Comput. Vision*, *73*(3), 263–284.
Müller, F., and C. M. Keeler (1969), Errors in short-term ablation measurements on melting ice surfaces, *J. Glaciol.*, *8*(52), 91–105.
Munro, D. S. (1989), Surface roughness and bulk heat transfer on a glacier: Comparison with eddy correlation, *J. Glaciol.*, *35*(121), 343–348.
Nield, J. M., R. C. Chiverrell, S. E. Darby, J. Leyland, L. H. Vircavs, and B. Jacobs (2012), Complex spatial feedbacks of tephra redistribution, ice melt and surface roughness modulate ablation on tephra covered glaciers, *Earth Surf. Processes Landforms*, *38*(1), 95–102.
Nield, J. M., et al. (2013), Estimating aerodynamic roughness over complex surface terrain, *J. Geophys. Res. Atmos.*, *118*, 12,948–12,961, doi:10.1002/2013JD020632.
Panofsky, H. A. (1984), Vertical variation of the roughness length at the boulder atmospheric observatory, *Boundary Layer Meteorol.*, *28*, 305–308.
Passalacqua, P., et al. (2015), Analyzing high resolution topography for advancing the understanding of mass and energy transfer through landscapes: A review, *Earth Sci. Rev.*, *148*, 174–193.
Powell, D. M. (2014), Flow resistance in gravel-bed rivers: Progress in research, *Earth Sci. Rev.*, *136*, 301–338.
Prandtl, L. (1926), Über die ausgebildete turbulenz, Verh. 2nd. Intl. Kong. Fur Tech. Mech. Zurich, (english translation, NACA technical memoir), 435, pp. 62–74.
Raupach, M. R. (1992), Drag and drag partition on rough surfaces, *Boundary Layer Meteorol.*, *60*, 375–395.
Rees, W. G., and N. S. Arnold (2006), Scale-dependent roughness of a glacier surface: Implications for radar backscatter and aerodynamic roughness modelling, *J. Glaciol.*, *52*, 214–222.
RIEGL (2012), Data Sheet Riegl VZ-1000. [Available at http://www.riegl.com/uploads/tx_pxpriegldownloads/DataSheet_VZ-1000_2015-03-24.pdf, (Date Accessed 21st August 2015).]
Rippin, D. M., A. Pomfret, and N. King (2015), High resolution mapping of supraglacial drainage pathways reveals link between micro-channel drainage density, surface roughness and surface reflectance, *Earth Surf. Processes Landforms*, doi:10.1002/esp.3719.
Ryan, J. C., A. L. Hubbard, J. E. Box, J. Todd, P. Christoffersen, J. R. Carr, T. O. Holt, and N. Snooke (2015), UAV photogrammetry and structure from motion to assess calving dynamics at Store Glacier, a large outlet draining the Greenland ice sheet, *Cryosphere*, *9*(1), 1–11.
Schürch, P., A. L. Densmore, N. J. Rosser, M. Lim, and B. W. McArdell (2011), Detection of surface change in complex topography using terrestrial laser scanning: Application to the Illgraben debris-flow channel, *Earth Surf. Processes Landforms*, *36*(14), 1847–1859.
Sellers, W. (1965), *Physical Climatology*, pp. 272, Univ. of Chicago Press, Chicago.
Sicart, J. E., M. Litt, W. Helgason, V. B. Tahar, and T. Chaperon (2014), A study of the atmospheric surface layer and roughness lengths on the high-altitude tropical Zongo glacier, Bolivia, *J. Geophys. Res. Atmos.*, *119*, 3793–3808, doi:10.1002/2013JD020615.
Smeets, C. J. P. P., and M. R. van den Broeke (2008), Temporal and spatial variations of the aerodynamic roughness length in the ablation zone of the Greenland ice sheet, *Boundary Layer Meteorol.*, *128*(3), 315–338.
Smeets, C. J. P. P., P. G. Duynkerke, and H. F. Vugts (1999), Observed wind profiles and turbulence fluxes over an ice surface with changing surface roughness, *Boundary Layer Meteorol.*, *92*(1), 101–123.

Smith, B. E., C. F. Raymond, and T. Scambos (2006), Anisotropic texture of ice sheets, *J. Geophys. Res.*, *111*, F01019, doi:10.1029/2005JF000393.
Smith, M. W. (2014), Roughness in the Earth sciences, *Earth Sci. Rev.*, *136*, 202–225, doi:10.1016/j.earscirev.2014.05.016.
Smith, M. W., and D. Vericat (2015), From experimental plots to experimental landscapes: Topography, erosion and deposition in sub-humid badlands from Structure-from-Motion photogrammetry, *Earth Surf. Processes Landforms*, *40*, 1656–1671.
Smith, M. W., J. L. Carrivick, and D. J. Quincey (2015), Structure from motion photogrammetry in physical geography, *Prog. Phys. Geogr.*, doi:10.1177/0309133315615805.
Sullivan, R., and R. Greeley (1993), Comparison of aerodynamic roughness measured in a field experiment and in a wind tunnel simulation, *J. Wind Eng. Ind. Aerodyn.*, *48*(1), 25–50.
Theurer, W. (1973), Dispersion of ground-level emissions in complex built-up areas, Ph.D. Thesis, University of Karlsruhe, Germany (in German).
van den Broeke, M. (1996), Characteristics of the lower ablation zone of the west Greenland ice sheet for energy-balance modelling, *Ann. Glaciol.*, *23*, 160–66.
Vericat, D., M. W. Smith, and J. Brasington (2014), Patterns of topographic change in sub-humid badlands determined by high resolution multi-temporal topographic surveys, *Catena*, *120*, 164–176.
Wallén, C. C. (1948), Glacial–meteorological investigations on the Karsa Glacier in Swedish Lappland, *Geogr. Ann.*, *30*(3–4), 451–672.
Wallén, C. C. (1949), Shrinkage of the Karsa Glacier and its probable meteorological causes, *Geogr. Ann.*, *31*(1–2), 275–291.
Wallén, C. C. (1959), The Karsa Glacier and its relation to the climate of the Torne Trask region, *Geogr. Ann.*, *41*(4), 236–244.
Wieringa, J. (1993), Representative roughness parameters for homogeneous terrain, *Boundary Layer Meteorol.*, *63*, 323–363.
Wooding, R. A., E. F. Bradley, and J. K. Marshall (1973), Drag due to regular arrays of roughness elements of varying geometry, *Boundary Layer Meteorol.*, *5*, 285–308.

Journal of Geophysical Research - Earth Surface

Supporting Information for

Aerodynamic roughness of glacial ice surfaces derived from high resolution topographic data

Mark W. Smith[1], Duncan J. Quincey[1], Timothy Dixon[2], Robert G. Bingham[3], Jonathan L. Carrivick[1], Tristram D. L. Irvine-Fynn[4], and David M. Rippin[5]

[1] School of Geography and water@leeds, University of Leeds, Leeds, UK, LS2 9JT
[2] School of Earth and Environment, University of Leeds, Leeds, UK, LS2 9JT
[3] School of GeoSciences, University of Edinburgh, Drummond Street, Edinburgh, UK, EH8 9XP
[4] Centre for Glaciology, Department for Geography and Earth Sciences, Aberystwyth University, Aberystwyth, UK, SY23 3DB
[5] Environment Department, University of York, Heslington, York, UK, YO10 5DD

Contents of this file

Introduction

This Supporting Information presents georeferencing, TLS validation and aerodynamic roughness height information for each plot examined. Data were collected and processed as described in the main text.

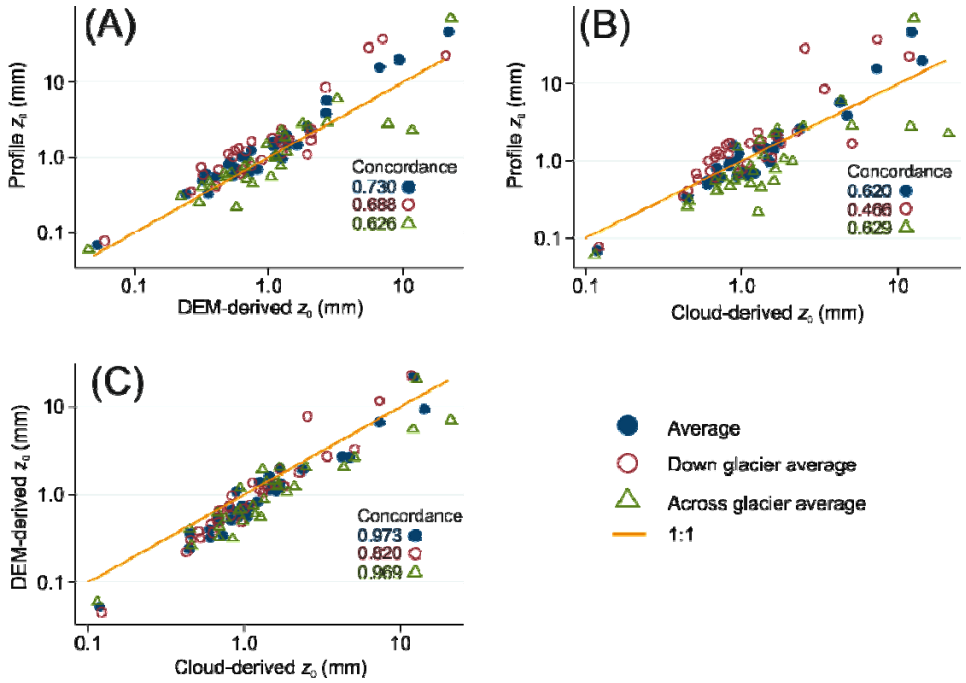

Figure S1. Comparison of z_0 values for each plot. Average z_0 represents the average for all directions, while down and across glacier averages are computed separately. Concordance values represent the concordance correlation between the two variables (as per Lin, 1989; 2000). Note the log-log scale.

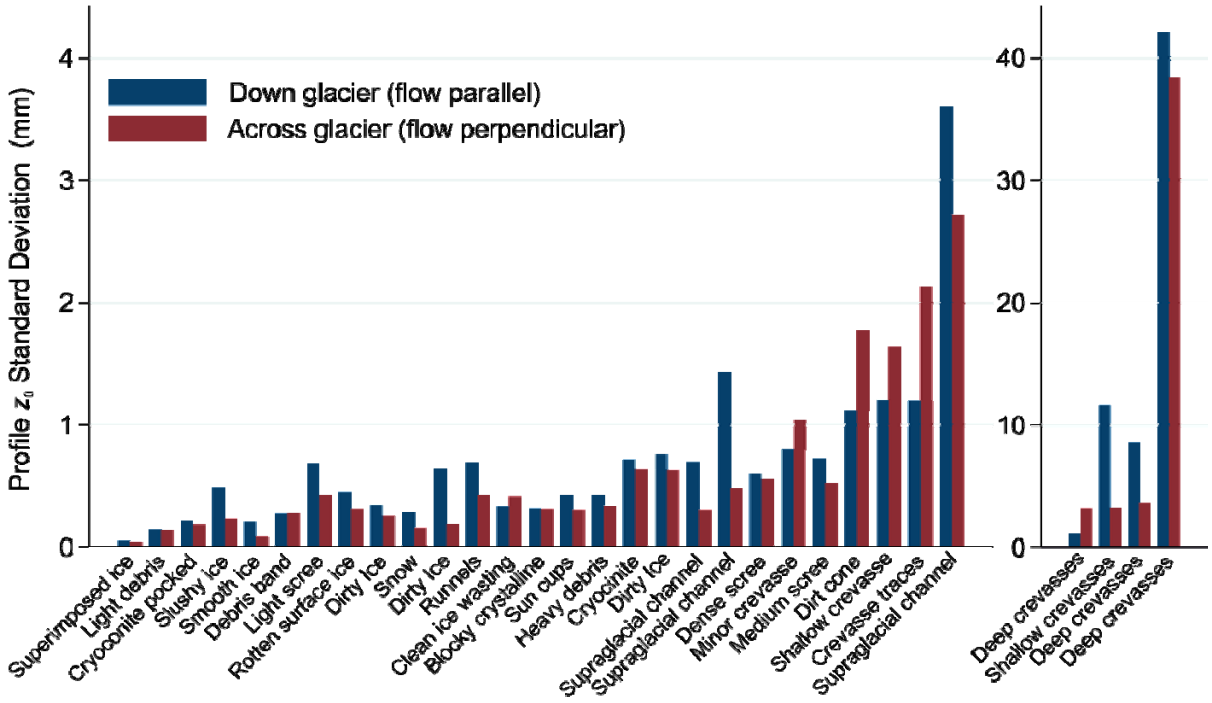

Figure S2. Standard deviation of profile z_0 values for each plot and each orthogonal direction.

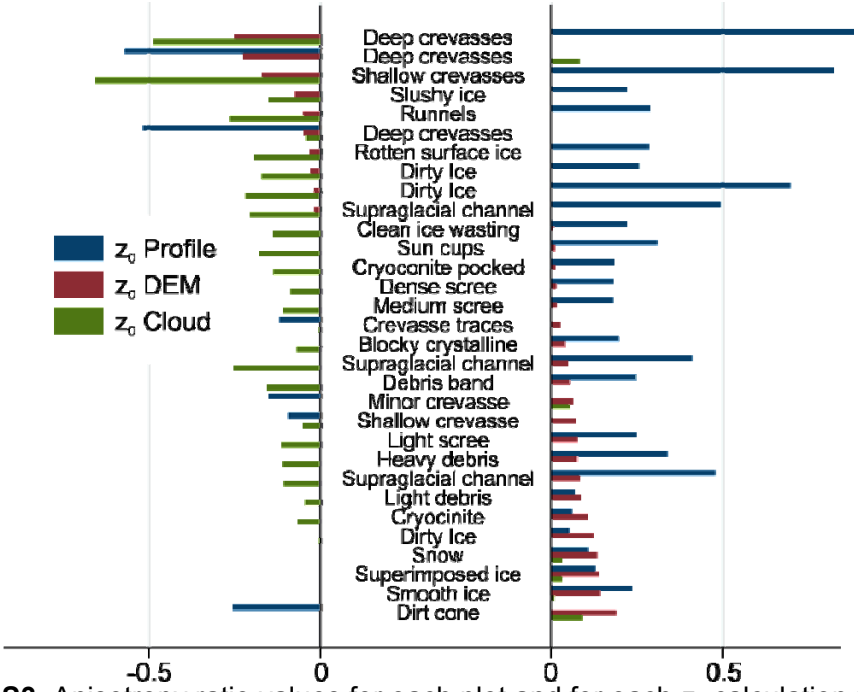

Figure S3. Anisotropy ratio values for each plot and for each z_0 calculation method (plots ordered by DEM-based z_0 values).

Plot ID	Description	Point Density (m^{-2})	3D Georeferencing error (mm)		TLS validation MAE (mm)	
			Non-optimized	Optimized	Non-optimized	Optimized
A	Supraglacial channel	282862	8.405	0.379	6.668	8.925
B	Runnels	275281	14.935	10.971	5.501	4.266
C	Snow	289410	15.471	3.301	5.105	4.786
D	Blocky crystalline	375784	16.705	0.037	4.801	6.559
E	Dirty Ice	312401	11.087	11.223	6.173	5.643
F	Shallow crevasses	225663	8.093	7.707		
G	Slushy ice	358993	6.5	6.341	6.587	6.56
H	Deep crevasses	230771	13.128	14.352	8.893	8.258
I	Deep crevasses	322504	9.812	10.562		
J	Shallow crevasse	396341	8.22	8.22	7.315	5.972
K	Supraglacial channel	295873	9.585	8.812	11.246	10.04
L	Clean ice wasting	300303	9.454	10.136	10.233	9.85
M	Dirty Ice	317497	15.474	0.857	6.644	8.212
N	Rotten surface ice	360942	5.413	0.08		
O	Light scree	355890	6.085	5.884	18.437	15.815
P	Medium scree	324199	17.89	0.472	9.051	7.951
Q	Dense scree	321946	17.104	17.878	13.675	15.453
R	Superimposed ice	391402	8.646	9.898		
S	Cryoconite pocked	408713	8.406	8.581	3.751	4.647
T	Debris band	319151	12.587	0.45	4.838	3.439
U	Smooth ice	355523	11.784	1.31	10.613	8.025
V	Crevasse traces	380704	12.227	0.452	7.067	5.333
W	Supraglacial channel	289100	8.613	9.651	6.554	6.677
X	Minor crevasse	324340	15.223	15.637	11.176	11.093
Y	Deep crevasses	28691	10.091	0.396	6.457	6.765
Z	Sun cups	339996	15.738	15.27	11.301	12.426
1	Cryocinite	368547	13.102	1.491	9.753	7.835
2	Heavy debris	325594	12.358	13.536	10.387	11.924
3	Dirt cone	320133	11.913	0.774	12.777	8.977
4	Dirty Ice	348169	10.179	0.331	5.993	5.084
5	Light debris	337123	7.97	0.193	9.158	11.045

Table S1.Summary of errors associated with each SfM plot survey (see Figure 1A for plot locations). TLS data were unavailable for four plots. Note that TLS validation data is not necessarily more accurate than SfM data given the respective survey ranges.

$n = 27$	MAE (mm)	SDE (mm)	RMSE (mm)
Non-Optimized	8.467	7.018	12.79
Optimized	8.138	7.323	12.85

Table S2. Mean error metrics for optimized and non-optimized SfM-MVS point clouds across 27 plots (four plots contained insufficient TLS validation points). Mean Absolute Error (MAE), Standard Deviation of Error (SDE) and Root Mean Square Error (RMSE) are presented.

Description	z_0 (mm)			Anisotropy Ratio		
	Profile	DEM	Cloud	Profile	DEM	Cloud
Supraglacial channel	1.673	1.180	1.678	0.409	0.048	-0.249
Runnels	1.019	0.629	0.929	0.287	-0.046	-0.261
Snow	0.625	0.561	0.925	0.109	0.132	0.029
Dirty Ice	1.419	1.092	1.597	0.255	-0.025	-0.169
Shallow crevasses	15.788	6.650	7.282	0.822	-0.166	-0.653
Deep crevasses	46.823	21.766	12.194	-0.513	-0.044	-0.037
Rotten surface ice	0.863	0.513	0.818	0.281	-0.026	-0.188
Light scree	0.803	0.500	0.684	0.246	0.075	-0.108
Medium scree	1.434	1.375	1.254	0.177	0.013	-0.103
Dense scree	0.947	1.243	1.511	0.178	0.013	-0.082
Crevasse traces	2.325	1.990	1.676	-0.114	0.026	-0.002
Supraglacial channel	5.704	2.685	4.222	0.493	-0.013	-0.199
Debris band	0.549	0.400	0.600	0.245	0.055	-0.151
Cryoconite pocked	0.491	0.321	0.602	0.183	0.011	-0.134
Smooth ice	0.331	0.352	0.449	0.234	0.142	0.007
Superimposed ice	0.068	0.053	0.118	0.125	0.138	0.031
Deep crevasses	3.852	2.656	4.696	-0.566	-0.223	0.080
Sun cups	1.240	0.739	0.961	0.308	0.011	-0.176
Cryocinite	1.595	1.077	0.884	0.060	0.103	-0.061
Heavy debris	0.687	0.820	1.204	0.337	0.077	-0.105
Light debris	0.326	0.242	0.440	0.068	0.087	-0.040
Minor crevasse	1.965	1.332	1.698	-0.145	0.063	0.051
Dirt cone	1.459	1.623	1.425	-0.252	0.189	0.088
Dirty Ice	0.570	0.547	0.674	0.050	0.123	0.003
Slushy ice	0.605	0.337	0.731	0.219	-0.070	-0.146
Blocky crystalline	0.638	0.714	1.067	0.196	0.040	-0.065
Deep crevasses	19.909	9.346	14.175	0.886	-0.247	-0.482
Shallow crevasse	2.597	1.919	2.353	-0.089	0.071	-0.046
Supraglacial channel	1.053	1.129	1.456	0.479	0.082	-0.102
Dirty Ice	0.717	0.565	1.044	0.696	-0.015	-0.216
Clean ice wasting	0.977	0.669	0.829	0.222	0.005	-0.135

Table S3. Summary of directionally-averaged z_0 values and anisotropy ratios for each plot and each calculation method.